

Published in final edited form as:

Biochemistry. 2011 June 14; 50(23): 5236–5248. doi:10.1021/bi2004119.

Two distinct ferritin-like molecules in *P. aeruginosa*: The product of the *bfrA* gene is a bacterial ferritin (FtnA) not a bacterioferritin (Bfr)^{†,€}

Huili Yao[‡], Grace Jepakorir[‡], Scott Lovell[§], Pavithra V. Nama[‡], Saroja Weeratunga[‡], Kevin P. Battaile[€], and Mario Rivera^{*‡}

[‡]Ralph N. Adams Institute for Bioanalytical Chemistry & Department of Chemistry, University of Kansas, Multidisciplinary Research Building, 2030 Becker Dr., Lawrence, KS 66047.

[§]Del Shankel Structural Biology Center, University of Kansas, 2034 Becker Dr., Lawrence, KS 66047.

[€]IMCA-CAT, Hauptman Woodward Medical Research Institute, Sector 17, APS Argonne National Laboratory, 9700 S. Cass Avenue, Bldg. 435A, Argonne, IL 60439.

Abstract

Two distinct types of ferritin-like molecules often coexist in bacteria, the heme binding bacterioferritins (Bfr) and the non-heme binding bacterial ferritins (Ftn). The early isolation of a ferritin-like molecule from *P. aeruginosa* suggested the possibility of a bacterioferritin assembled from two different subunits [Moore, G. R., Kadir, F. H., Al-Massad, F. K., Le Brun, N. E., Thomson, A. J., Greenwood, C., Keen, J. N. and Findlay, J. B. C. (1994) *Biochem. J.* 304, 493–497]. Subsequent studies demonstrated the presence of two genes coding for ferritin-like molecules in *P. aeruginosa*, designated *bfrA* and *bfrB*, and suggested that two distinct bacterioferritins may coexist [Ma, J.-F., Ochsner, U. A., Klotz, M. G., Nanayakkara, V. K., Howell, M. L., Johnson, Z., Posey, J. E., Vasil, M. L., Monaco, J. J., and Hassett, D. J. (1999) *J. Bacteriol.* 181, 3730–3742]. In this report we present structural evidence demonstrating that the product of the *bfrA* gene is a ferritin-like molecule not capable of binding heme which harbors a catalytically active ferroxidase center with structural properties similar to those characteristic of bacterial and archaeal Ftns and clearly distinct from the ferroxidase center typical of Bfrs. Consequently, the product of the *bfrA* gene in *P. aeruginosa* is a bacterial ferritin, which we propose should be termed *Pa* FtnA. These results, together with the previous characterization of the product of the *bfrB* gene as a genuine bacterioferritin (*Pa* BfrB) [Weeratunga, S. J., Lovell, S., Yao, H., Battaile, K. P., Fischer, C. J., Gee, C. E., and Rivera, M. (2010) *Biochemistry* 49, 1160–1175] indicate the coexistence of a bacterial ferritin (*Pa* FtnA) and a bacterioferritin (*Pa* BfrB) in *P. aeruginosa*. In agreement with this idea, we also obtained evidence demonstrating that release

[†]This work was supported by grants from the National Science Foundation (MCB-0818488), the National Institute of Health, GM-50503 and P20 RR-17708 from the National Center for Research Resources.

[€]Coordinates and crystallographic structure factors for the distinct *Pa* FtnA structures have been deposited in the protein data bank under accession codes 3R2O (as isolated pH 6.0), 3R2K (as isolated pH 7.5), 3R2H (as isolated pH 10.5), 3R2R (Fe soaked, pH 6.0), 3R2L (Fe soaked, pH 7.5), 3R2S (double soaked, pH 6.0) and 3R2M (double soaked, pH 7.5).

*Corresponding author: Mario Rivera, Ralph N. Adams Institute for Bioanalytical Chemistry & Department of Chemistry, University of Kansas, Multidisciplinary Research Building, 2030 Becker Dr., Lawrence, KS 66047. Telephone: 785-864-4936; Fax: 785-864-1916; mrivera@ku.edu.

SUPPORTING INFORMATION

Amino acid sequence of the protein coded by the *P. aeruginosa* *bfrA* gene (*Pa* FtnA) aligned against the amino acid sequences of bacterioferritins of known structure; 2Fo-Fc electron density maps of the ferroxidase center ligands of *Pa* FtnA Fe soaked and double soaked; conformational changes in the *Pa* FtnA ferroxidase center upon binding iron; anomalous difference map showing sulfate in a 3-fold pore. This material is available free of charge via the Internet at <http://pubs.acs.org>

of iron from *Pa* BfrB and *Pa* FtnA is likely subject to different regulation in *P. aeruginosa*: Whereas the efficient release of iron stored in *Pa* FtnA requires only the input of electrons from a ferredoxin NADP reductase (*Pa* Fpr), the release of iron stored in *Pa* BfrB requires not only electron delivery by *Pa* Fpr, but the presence of a “regulator”, the apo form of a bacterioferritin-associated ferredoxin (*Pa* apo Bfd). Finally, structural analysis of iron uptake *in crystallo* suggests a possible pathway for the internalization of ferroxidase iron into the interior cavity of *Pa* FtnA.

Bacteria have developed several strategies to acquire and manage iron which include: (1) Deployment of molecules with high affinity for iron or heme to scavenge iron from the surroundings (1–4), (2) storage of intracellular iron to provide a source of the nutrient when external supplies become limited (5–7), (3) employment of redox stress resistance systems to minimize damage caused by iron-induced reactive oxygen species (8, 9) and (4) appropriate regulation of the expression of iron-binding proteins to meet the availability of iron (10). In *P. aeruginosa* and in many other pathogens these events are regulated by Fur, the master Fe uptake regulator (11), and by regulatory small RNAs (12). Significant advances have improved our understanding of the process of iron and heme-iron uptake by *P. aeruginosa* and other pathogens (13–18). In comparison, how the cell enables the utilization of its intracellular iron while avoiding iron toxicity remains to be understood. One mechanism whereby iron toxicity can be ameliorated or controlled is by storage of excess iron in ferritin and ferritin-like molecules. These molecules function by oxidizing Fe²⁺ using O₂ and H₂O₂ as electron acceptors and internalize the resultant Fe³⁺ in the form of a mineral. When environmental iron concentrations are low, Fe³⁺ stored in ferritin-like molecules is mobilized for its incorporation in metabolism, which is why ferritin-like molecules act as dynamic regulators of cytosolic iron concentrations.

Ferritin-like molecules are found in eukaryotes and prokaryotes (6). Eukaryotic ferritins are composed of two different but isostructural subunit types, H and L, which assemble into a 24-mer structure (19). In comparison, two types of ferritin-like molecules can be found in bacteria, the ferritins (Ftn) and the bacterioferritins (Bfr) (5, 6). Ftns are composed of 24 subunits that assemble into a spherical protein shell surrounding a central cavity where the iron mineral is stored. Each subunit consists of a four-helix bundle and a short C'-terminal helix that is nearly perpendicular to the axis of the bundle. The hollow interior of ferritin-like molecules provides a large cavity for the storage of iron in the form of a ferric mineral, which can be made of as many as ~4500 iron atoms. The protein cage maintains the ferric mineral soluble and appears to isolate it from participating in redox reactions that may cause oxidative stress. A hallmark of the bacterioferritin structure is the presence of heme groups (20, 21). In all bacterioferritins of known structure, each heme is located on a two-fold symmetric axis within a subunit dimer, where it is axially coordinated by M⁵² from each subunit. Hence, twelve subunit dimers assemble to form the Bfr structure containing 12 heme molecules. The heme iron plays a key role in mediating electrons across the protein coat to reduce the ferric iron mineral, previous to its release for incorporation in metabolism (22).

Ferritin-like molecules take soluble Fe²⁺ and store it as a ferric (Fe³⁺) mineral, which means that the iron storage process requires a ferroxidation step. This process is catalyzed by specific sites in the protein called ferroxidase centers, which in bacterial Ftn and in Bfr are located in the middle of each subunit (23). Despite the central role played by the ferroxidase center in the process of iron uptake, its structure is not conserved amongst eukaryotic, bacterial and bacterioferritins. Available structures, however, suggest significant structural conservation of ferroxidase centers among Ftns and amongst Bfrs. The main structural differences between ferroxidase centers in eukaryotic Ftn, Bfr and bacterial Ftn are illustrated in Figure 1: The ferroxidase center of Bfr is highly symmetrical (24–28), with

each of the iron ions (Fe_1 and Fe_2) coordinated by two bridging glutamates and by His and Glu residues as capping ligands (Figure 1-A). In the ferroxidase center of bacterial and archaeal Ftns of known structure, Fe_A and Fe_B are bridged by only one protein-provided ligand (29–32) (Figure 1-B). In this context, the ferroxidase center of bacterial Ftns is more similar to the ferroxidase center of eukaryotic Ftns (Figure 1-C) than to the ferroxidase center of Bfrs. An interesting feature of bacterial Ftn is the presence of an additional iron near the ferroxidase center (29). This site, also observed in the ferroxidase center of *Pyrococcus furiosus* (31) and *Archaeoglobus fulgidus* (32) ferritins, has been termed “site C”, and is not essential for iron mineralization but appears to exert influence in the process of moving iron into the protein cavity (21, 33).

Early studies reported that bacterioferritin isolated from *P. aeruginosa* seemed to be heterogeneous and consist of two types of subunits, α and β , which were found to be present in different proportions, depending on the sample (34, 35). Subsequent investigations established two genes coding for ferritin-like molecules in *P. aeruginosa*, termed *bfrA* and *bfrB* (9) under the assumption that they code for two bacterioferritins, BfrA and BfrB. An amino acid sequence alignment comparing the amino acid sequence of the protein coded by the *bfrA* gene with those corresponding to bacterioferritins of known structure (Figure S1) shows that M^{52} is absent from the amino acid sequence encoded by *bfrA*. Absence of M^{52} in the sequence of the *bfrA* product may render this protein incapable of binding heme, which led us to hypothesize that the *bfrA* gene codes for a bacterial ferritin (Ftn), not a bacterioferritin (Bfr) (22). The implication of this notion is that iron storage and management in the cytosol of *P. aeruginosa* is carried out by a bacterial ferritin (Ftn) and a bacterioferritin (Bfr), instead of a single bacterioferritin composed of two distinct subunits.

Available genetic information supports the idea of two ferritin-like molecules functioning independently in *P. aeruginosa*: In *E. coli*, *P. aeruginosa* and in other organisms, the *bfrB* gene is next to a *bfd* gene, which codes for a bacterioferritin-associated ferredoxin (36–39). In *P. aeruginosa* iron starvation causes negative regulation of the *bfrB* gene (40) and strong positive regulation of the *bfd* gene (41). In vitro, the efficient mobilization of iron from *Pa* BfrB requires the presence of apo *Pa* Bfd and delivery of electrons from *Pa* Fpr, which suggests that apo *Pa* Bfd acts as a regulator in the release of iron from *Pa* BfrB (22). In *P. aeruginosa* the *bfrA* gene is adjacent to a *kata* gene, which codes for a catalase active in all growth phases. A *bfrA* mutant of *P. aeruginosa* was found to express only 50% of the catalase activity of wild type cells, while in contrast, a *bfrB* mutant did not have any effect on the catalase activity of the cell (9). These observations taken together support the notion that the products of the *bfrA* and *bfrB* genes assemble into independent ferritin-like molecules that play different, or redundant but independent roles in iron management.

To challenge the idea that iron metabolism in *P. aeruginosa* is aided by one bacterial ferritin and one bacterioferritin, rather than by a unique heterogeneous bacterioferritin, we have undertaken the biochemical and structural characterization of the proteins coded by the *bfrA* and *bfrB* genes. In previous reports we showed that the product of the *bfrB* gene (*Pa* BfrB) is a genuine bacterioferritin assembled from 24 identical subunits and 12 heme molecules which harbors a symmetrical ferroxidase center typical of Bfr (22, 24). Herein, we report that the product of the *bfrA* gene is a protein assembled from 24 identical subunits that can't bind heme. Its ferroxidase center is reminiscent of those typical of bacterial ferritins (Ftn) and is clearly distinct from the ferroxidase center of bacterioferritins. Hence, the structure of the so called bacterioferritin A (BfrA) in *P. aeruginosa* reveals that this protein is a bacterial ferritin, and we propose that it should be termed *Pa* FtnA. We also found that iron release from *Pa* BfrB and *Pa* FtnA have different requirements: Whereas iron release from *Pa* BfrB requires the presence of a regulator (*Pa* Bfd) in addition to electrons supplied by a reductase (22), iron release from *Pa* FtnA requires only electron delivery from a reductase.

These structural and functional properties, together with the available genetic information, strongly support the presence of two ferritin-like molecules in *P. aeruginosa*, a bacterial ferritin (*Pa FtnA*) and a bacterioferritin (*Pa BfrB*).

MATERIALS AND METHODS

Cloning of *P. aeruginosa bfrA*

The gene encoding for *Pa FtnA* (PA4235) was synthesized, subcloned into a pET11a vector, and sequenced (GeneScript Corp., Piscataway, NJ). The gene was engineered with silent mutations introducing codons favored by *E. coli* (42) and with *NdeI* and *BamHI* restriction sites at the 5' and 3' ends, respectively, for subcloning. The pET11a/*bfrA* construct was transformed into *E. coli* BL21DE3 Gold cells (Stratagene) for protein expression.

Expression and Purification of *Pa FtnA*

A single colony of *E. coli* BL21(DE3) competent cells harboring the recombinant pET11a-*bfrA* construct was cultured overnight at 37 °C in 50 mL of LB medium containing 100 µg/mL ampicillin. The 50 mL culture was used to inoculate 1 L of fresh LB medium (100 µg/mL ampicillin) which was shake-incubated (200 rpm) until the optical density at 600 nm (OD₆₀₀) was 0.6. The temperature was then lowered to 30 °C and the culture was allowed to reach an OD₆₀₀ of 0.8 before protein expression was induced by addition of IPTG (isopropyl 1-thio-D-galactopyranoside) to a final concentration of 1 mM. Cells were cultured for an additional 4 h at 30 °C before they were harvested by centrifugation and stored at -20 °C. Cell paste was resuspended (3 mL/g of cell paste) in 50 mM Tris-Base buffer, pH 7.6, containing 10 mM EDTA, 0.5 mM PMSF, protease inhibitor cocktail (Sigma Aldrich) and DNase (Sigma Aldrich) and were lysed using a constant cell disruptor at 20 psi. Cell debris were pelleted by centrifugation at 4 °C and 19,500 rpm for 45 min and the supernatant was loaded onto a Q-Sepharose fast flow column (12 cm × 2.5 cm i.d.) equilibrated with 20 mM Tris-Base, 1 mM EDTA, pH 7.6 at 4 °C. The column was washed with 3 bed volumes of the same buffer and the protein was eluted with a linear gradient (0–600 mM) of NaCl. Fractions containing *Pa FtnA* were pooled and dialyzed against 4 L of 20 mM Tris-HCl, 1 mM EDTA, pH 7.6 at 4 °C and the resultant solution loaded onto a second Q-Sepharose fast flow column (12 cm × 2.5 cm i.d.) and eluted as described above. Fractions containing *Pa FtnA* were pooled and NaCl was added to a final concentration of ~ 500 mM, to prevent protein precipitation during concentration by ultrafiltration (Ultracel 50K; Millipore). The concentrated solution (~ 4 mL) was loaded onto Sephacryl S-300 (GE Healthcare) size exclusion column (90 cm × 2.5 cm i.d.) equilibrated with 50 mM Tris-HCl, 200 mM NaCl, 1 mM EDTA, pH 7.6 at 4 °C. Fractions containing *Pa FtnA* were pooled, concentrated and then loaded a second time onto the Sephacryl S-300 column, which typically resulted in homogenous protein, as judged by SDS-PAGE (15%). In some preparations it was necessary to pass the sample a third time through the Sephacryl S-300 column to obtain pure *Pa FtnA*.

The molecular mass of a *Pa-FtnA* subunit was obtained by mass spectrometry using an ESI-MS Q-TOF mass spectrometer (Micromass Ltd, Manchester UK). To this end, a 5 µM sample of *Pa FtnA* in 50 mM phosphate buffer, pH 7.4 was loaded onto a 0.5 mm i.d. C4 reverse phase column (MC-5-C4 300 Å pore size, Micro Tech). Elution was carried out by running an acetonitrile/isopropyl alcohol/water linear gradient of 4% acetonitrile/min at 10 µL/min from 20% to 60% acetonitrile (buffer A: 99% water, 1% acetonitrile, 0.08% formic acid; buffer B: 80% acetonitrile, 10% isopropyl alcohol, 10% water, 0.06% formic acid). The molecular mass of 24-mer *Pa-FtnA* was estimated by FPLC (AKTA, Amersham Pharmacia Biotech) using a size exclusion column (Superdex 200 Prep., 60 cm × 16 cm i.d. (GE Healthcare), equilibrated with 50 mM sodium phosphate (pH 7.4), 150 mM NaCl and 1 mM TCEP. The column was calibrated with a set of molecular mass standards (GE

Healthcare) that included ferritin (440,000 Da), aldolase (158,000 Da), conalbumin (75,000 Da), and carbonic anhydrase (29,000 Da).

Loading *Pa* FtnA with iron

Recombinant *Pa* FtnA, as isolated, contains a small amount of iron in its core, ~10–15 iron ions per *Pa* FtnA 24-mer. To load *Pa* FtnA with iron, a solution of ferrous ammonium sulfate was prepared in a glove box (Coy Laboratories), placed in a container capped with a rubber septum, and removed from the anaerobic chamber. Concentrated HCl was added to the ferrous ammonium sulfate solution (50 μ L/100 mL) through a septum using a Hamilton microsyringe needle; the resultant solution was added to a stirred solution of 0.2 μ M *Pa* FtnA in 50 mM TRIS, pH 7.4 at ambient temperature. Aliquots, which delivered approximately 10% of the total iron necessary to load each *Pa* FtnA molecule with ~500 iron ions, were added approximately 15 min apart. The content of iron in the core was determined using a previously reported method (22, 43). A similar procedure (22) was used to load *Pa* BfrB with ~550 iron ions.

Iron Release from the core of *Pa* FtnA and *Pa* BfrB

To study the release of iron stored in *Pa* FtnA and *Pa* BfrB the proteins were mineralized with ~ 500 iron ions and placed in an anaerobic glove box (22). Experiments to investigate the release of iron stored in *Pa* FtnA and *Pa* BfrB were carried out in the same anaerobic chamber, in a manner analogous to that reported previously for the release of iron from *Pa* BfrB (22). Reactions were carried out in a 1.0 cm path-length cuvette equipped with a magnetic stirring bar and containing a 3 mM solution of 2,2'-bipyridyl (bipy) in 20 mM potassium phosphate, pH 7.6. For the study of *Pa* FtnA, a few microliters from a stock solution of *Pa* FtnA and *Pa* Fpr was added to the cuvette to make the solution 0.25 μ M in *Pa* FtnA and 10 μ M in *Pa* Fpr. The reaction was initiated by addition of excess NADPH to a final concentration of 1.5 mM and the progress monitored by following the time-dependent changes in the intensity of the band at 523 nm upon formation of the $[\text{Fe}(\text{bipy})_3]^{2+}$ complex. A similar procedure was used to study iron release from *Pa* BfrB, except that the cuvette also contained apo *Pa* Bfd, in concentrations described in the caption to Figure 9. Apo *Pa* Bfd was prepared in situ from holo *Pa* Bfd, using a procedure described previously (22). In short, holo *Pa* Bfd was added to a stirred cuvette containing 3 mM bipy in 20 mM potassium phosphate, pH 7.6. Sodium dithionite (5 mM) was added to stoichiometrically reduce the Fe^{3+} in holo *Pa* Bfd to Fe^{2+} . Capturing of the ferrous ion by bipy was monitored by the time-dependent increase in the 523 nm absorbance, which was followed until it reached a plateau with intensity corresponding to the theoretical value calculated from the amount of holo *Pa* Bfd placed in the cuvette. At this point, the solution containing apo *Pa* Bfd was reconstituted with *Pa* Fpr and *Pa* BfrB and the iron mobilization reaction initiated by the addition of NADPH, as described above. Experiments involving apo *Pa* Bfd and *Pa* FtnA were carried in an analogous manner. Please note that throughout these studies, Bfd stands for the C43S mutant of Bfd, which has previously been shown to behave like wild type Bfd, but can be expressed in higher yield and is more stable to storage and manipulation (22).

Crystallization and data collection

Pa FtnA was concentrated to 8.0 mg/mL in 100 mM Tris buffer, pH 7.6, containing 200 mM NaCl and 1 mM EDTA for crystallization. Crystals were grown under aerobic conditions in Compact Jr. sitting-drop vapor diffusion plates (Emerald Biosystems) using 0.5 μ L of protein and 0.5 μ L of crystallization solution equilibrated against 100 μ L of the latter. Crystals were obtained from three different conditions at 20 °C: (a) pH 6.0 crystals were obtained from Wizard2 #2 (Emerald Biosystems), 35% (v/v) 2-methyl-2,4-pentanediol, 100 mM MES pH 6.0, 200 mM Li_2SO_4 . Crystals were transferred to a fresh drop of

crystallization solution, which served as cryoprotectant prior to freezing in liquid nitrogen for data acquisition. (b) pH 7.5 crystals were obtained from Wizard 2 #5 (Emerald Biosystems) 20% (v/v) 1,4-butanediol, 100 mM HEPES pH 7.5, 200 mM NaCl. Crystals were transferred to a solution containing 80% crystallization solution and 20% glycerol for approximately 30 s before freezing in liquid nitrogen for data collection. (c) pH 10.5 crystals were obtained from Wizard 2 #39 (Emerald Biosystems), 20% (w/v) PEG-8000, 100 mM CAPS pH 10.5, 200 mM NaCl. Crystals were transferred to a solution containing 80% crystallization solution and 20% PEG400 for approximately 30 s before freezing in liquid nitrogen for data collection. To prepare samples with iron bound in the ferroxidase center, crystals obtained at each of the three pH values were soaked aerobically for 15 min in their respective crystallization solution containing 50 mM FeCl₂. Doubly soaked crystals were prepared by aerobically soaking crystals in 50 mM FeCl₂ for 15 min, followed by aerobically soaking for 30 min in the same crystallization solution without FeCl₂. Single crystals at each of the pH values were transferred to the corresponding cryoprotection solution described above before freezing in liquid nitrogen for data collection. X-ray diffraction data were collected at 100 K at the Advanced Photon Source (APS) IMCA-CAT, sector 17-BM, using an ADSC Quantum 210 CCD detector for apo pH 10.5 crystals at a λ of 1.0000 Å. Diffraction data for apo (pH 7.5) and Fe soaked (pH 7.5) crystals were collected using a Mar 165 CCD detector at wavelengths $\lambda = 1.0000$ and 1.6531 Å. Data at 1.6531 Å were collected to obtain an anomalous signal from potentially bound Fe ions. Although the X-ray fluorescence K-edge emission peak of Fe has a maximum at approximately 1.74 Å, at 1.6314 Å prominent anomalous signals can be observed for Fe ions. Data for pH 6.0 and double soaked pH 7.5 Pa FtnA crystals were collected at the APS sector 17-ID using a Pilatus 6M pixel array detector at $\lambda = 1.7401$ Å, which was at the Fe absorption edge.

Structure solution and refinement

Intensities for as-isolated (pH 7.5) and Fe soaked (pH 7.5) data sets were integrated and scaled using the HKL2000 package (44). Intensities for all other data sets were integrated and scaled using the XDS (45) and Scala (46) packages respectively. Initial structure solution was carried out by molecular replacement, using the as isolated (pH 10.5) data set, with Molrep (47) using a single subunit of *Pa* BfrB (PDB: 3IS7) as the search model. The top solution yielding the highest correlation coefficient was obtained for a single monomer in the asymmetric unit in the space group *F*432. The final *Pa* FtnA model obtained from the as isolated pH 10.5 data was used for subsequent molecular replacement searches against all other data sets. Structure refinement and manual model building were performed with Phenix (48) and Coot (49), respectively. Structure validation was performed using Molprobity (50) and figures were prepared with CCP4mg (51).

Following initial refinement, certain iron atoms, for a particular structure, contained negative electron density (Fo-Fc) and *B*-factors that were approximately twice that of the Fe_A site. The anomalous difference maps were examined and peak heights and *B*-factors of the Fe atoms were compared for each particular structure. Occupancy factors were manually adjusted to values ranging from ~0.3 to ~0.5 (see below), the structures refined and the electron density maps and *B*-factors analyzed. Occupancies for the Fe ions were set as follows: (i) Fe Soaked (pH 6.0): the anomalous peak heights were similar for all iron atoms and were therefore refined with full occupancy factors. (ii) Double soak (pH 6.0): anomalous density peak heights for the Fe sites were 43.2 σ (Fe_A), 19.6 σ (Fe_B), 22.7 σ Fe_C and 20.7 σ (Fe_{His130}). Assuming an occupancy factor of 1.0 for Fe_A, all other Fe atoms were refined with 0.5 occupancy factors. (iii) Fe Soak (pH 7.5): anomalous peak heights were 20.6 σ (Fe_A), 21.1 σ (Fe_B) and approximately 8 σ for the sites Fe_C, Fe_D and Fe_E, thus sites Fe_C to Fe_E were refined with occupancy factors of 0.5. (iv) Double soaked (pH 7.5): anomalous peak heights were 45.5 σ (Fe_A), 42.1 σ (Fe_B) and 20.4 σ for Fe_C, so the latter was

refined with an occupancy factor of 0.5. Automated refinement of the occupancies for partially occupied Fe ions along with the *B*-factors in Phenix resulted in occupancy factors that were similar to those determined manually (approximately 0.5).

RESULTS

Overexpression, Purification and Characterization of *Pa* FtnA

Recombinant FtnA expressed in *E. coli* BL21DE3 cells was purified to homogeneity, as determined by the presence of a single band (~ 18 kDa) in a SDS-PAGE gel (Figure 2-A). The MW of a subunit was determined by electrospray ionization mass spectrometry to be 17,939 Da, a value in excellent agreement with that calculated from the amino acid sequence (17,940 Da), including the initiator methionine. The elution volume (V_e) of *Pa* FtnA from a calibrated size exclusion column is nearly identical to the V_e of a (eukaryotic) ferritin standard purchased from GE Healthcare (Figure 2-B). The molecular weight of FtnA, estimated from its V_e (436.3 kDa) is in good agreement with the 430.6 kDa value calculated from the amino acid sequence, thus demonstrating the structural integrity of the 24-mer FtnA assembly.

Preparation of iron-loaded *Pa* FtnA

Protein containing ~ 520 ± 20 iron atoms per *Pa* FtnA molecule was prepared by titrating an anaerobic solution of Fe²⁺ into a solution of *Pa* FtnA in air. As described previously for the mineralization of *Pa* BfrB (22), aliquots of Fe²⁺, each containing ~ 10% of the total iron, were added approximately 15 min apart to allow for uptake and mineralization. The corresponding spectra (Figure 2-C) show gradual increase in the absorption ca. 280 nm with good preservation of baseline, which indicates that the capture of Fe²⁺, and its subsequent oxidation and mineralization, are efficiently carried out by *Pa* FtnA.

X-ray crystallography

Crystals of *Pa* FtnA were obtained at pH 6.0, 7.5 and 10.5. Diffraction data were collected from crystals grown at each of the pH values from protein as-isolated (as-isolated *Pa* FtnA), after soaking crystals of as-isolated *Pa* FtnA in a solution of FeCl₂ dissolved in crystallization solution (Fe-soaked *Pa* FtnA) and after soaking crystals of Fe-soaked *Pa* FtnA in crystallization solution in the absence of FeCl₂ (double soaked *Pa* FtnA). The relevant crystallographic data are summarized in Table 1. The overall structures obtained from crystals at pH 6.0 and 7.5 and 10.5 are nearly identical; small but important and informative differences occur at the ferroxidase center in the Fe-soaked and double soaked structures. These differences will be discussed below, after we present relevant information obtained from the overall fold.

The *Pa* FtnA structure conforms to the fold typical of ferritin-like molecules and consists of an assembly of 24 identical subunits forming a nearly spherical shape with 4,3,2 point symmetry. The fold of each *Pa* FtnA subunit consists of a 4- α -helix bundle (helices A–D) and a fifth, short α -helix (E) that is nearly perpendicular to the four helix bundle (Figure 3-A). Figure 3-B shows a superposition of a *Pa* FtnA dimer (magenta) with its equivalent in *Pa* BfrB (blue) viewed along the two fold axis of symmetry, which passes through the heme iron. Evidently, the folds are nearly identical, except for the fact that *Pa* FtnA does not contain heme. In *Pa* BfrB and in all bacterioferritins of known structure, the axial ligands coordinating a heme molecule are two M⁵² side chains, one from each subunit in a dimer. Each M⁵² can axially coordinate the heme iron because their location at the center of the B helix place them relative close to one another and in an ideal geometry (collinear with the C₂ axis) to bind each of the two axial sites of a heme molecule (blue in Figure 3-C). In contrast, and due to the two-fold symmetry of a subunit dimer, residues located at either side of the

center of the B-helix become increasingly separated from one another and therefore incapable of acting as heme axial ligands. In the amino acid sequence of *Pa* FtnA position 52 (center of helix B) is occupied by Thr. The Met residue closest to the center of the B-helix is M⁴⁸ (magenta in Figure 3-C); its position, relatively far from the C₂ axis, preclude the M⁴⁸ side chains in a dimer from functioning as axial ligands to the heme iron. These structural observations, which are consistent with the absence of heme in *Pa* FtnA, clearly demonstrate that it did not evolve to bind heme, a property that relates it to bacterial ferritins and clearly separates it from bacterioferritins.

The ferroxidase center in as-isolated *Pa* FtnA is empty

As isolated, recombinant *Pa* FtnA (pH 6.0, pH 7.5 or pH 10.5) does not have iron in the ferroxidase center. Prominent difference electron density was observed in the ferroxidase center of the pH 10.5 structure but structural refinement that included Fe or water molecules in the model resulted in residual negative and positive difference density, respectively. A model that includes sodium ions, on the other hand, refined to an R factor of 15.3 and satisfied coordination geometry and bond lengths to respective ligands. Hence, the prominent difference electron density in the ferroxidase center of as isolated *Pa* FtnA (pH 10.5) most likely corresponds to two sodium ions (green Figure 4). E¹⁸ and H⁵⁴ serve as capping ligands to Na₁, E⁵¹ as a bridging ligand and E⁹³ as a capping ligand to Na₂ (green in Figure 4); the side chain of H¹³⁰ is rotated away from Na₂ in a conformation very similar to the “gate open” conformation of H¹³⁰ in the ferroxidase empty structure of *Pa* BfrB (24). The ferroxidase center in the pH 7.5 structure (magenta in Figure 4) also harbors two sodium ions in very similar positions. In addition, no anomalous difference electron density was observed in the ferroxidase center using diffraction data collected near the Fe absorption edge. H¹³⁰ in this structure is rotated toward Na₂, but does not bind it, whereas the side chain of E¹⁸ is in two conformations, one coordinates Na₁ and the other is rotated away from it. In the pH 6.0 structure (cyan in Figure 4) the ferroxidase center is devoid of metal ions, and the side chains of E¹⁸ and E⁹³ are rotated away from the positions occupied by Na₁ and Na₂ in the pH 7.5 and 10.5 structures. These conformational changes, which in the crystal structures are likely “snapshots” of predominant populations, suggest a dynamic ferroxidase center tuned to respond to changes in coordination state and local pH.

The iron-loaded ferroxidase center of *Pa* FtnA

Soaking crystals of as isolated *Pa* FtnA in crystallization solution containing 50 mM FeCl₂ (pH 6.0 and 7.5), followed by collection of X-ray diffraction data, resulted in structures with iron at the ferroxidase center; soaking crystals grown at pH 10.5 resulted in precipitation of the FeCl₂. Figure 5-A shows a zoomed-in view of the ferroxidase center in the *Pa* FtnA structure (pH 6.0) where Fe_A and Fe_B (orange) are coordinated by capping ligands E¹⁸ and H⁵⁴, and E⁹³ and H¹³⁰, respectively, and bridged by E⁵¹ and by a water molecule (red). The presence of iron is corroborated in the prominent difference electron density (F_o - F_c) and by the strong anomalous signal (blue mesh) from data acquired at 1.7401 Å. An identical view depicting 2Fo-Fc electron density maps of ferroxidase iron ligands is shown in Figure S2. The architecture of the *Pa* FtnA ferroxidase center, with only one bridging ligand provided by the protein is reminiscent of bacterial and eukaryotic ferritins and clearly distinct from the ferroxidase center of bacterioferritins (see Figure 1). The view of Figure 5-A also shows the presence of a third iron ion (Fe_C), which is coordinated by H⁴⁶, E⁵⁰ and four water molecules. This iron ion is similar to “site C” iron, first observed in the iron-soaked structure of *E. coli* FtnA (29) and subsequently in the Ftn proteins of *A. fulgidis* (31) and *P. furiosus* (32). An interesting distinction is that in *Pa* FtnA H¹³⁰ acts exclusively as a capping ligand to Fe_B, whereas in the ferroxidase center of *E. coli*, *A. fulgidis* and *P. furiosus* Ftn, the equivalent capping ligand, E¹³⁰, also coordinates Fe_C. Hence, the unique presence of His at position 130, not only constitutes a new Ftn ferroxidase center architecture, but also

represents a unique binding mode of Fe at “site C”. This structure (pH 6.0) was refined with full-occupancy factors for all three types of iron (see Methods).

Superposition of the full (cyan) and apo (purple) ferroxidase centers (pH 6.0), illustrates the conformational rearrangement in the side chains of E¹⁸ and E⁹³ and the minimal changes in the side chains of E⁵¹, H⁵⁴ and H¹³⁰ upon binding iron (Figure S3). Similar observations are made when comparing the ferroxidase full and empty structures obtained at pH 7.5, where the most significant change is the collapse of the two alternative conformations of the E¹⁸ side chain into one, iron bound conformation.

A similar view of the ferroxidase center in the iron soaked pH 7.5 structure (Figure 5-B) shows the presence of three iron ions, Fe_C, Fe_D and Fe_E in addition to Fe_A and Fe_B. These additional iron ions exhibit anomalous peak intensities approximately one half the peak intensities exhibited by Fe_A and Fe_B. Hence, as described in Methods, Fe_C, Fe_D and Fe_E were refined assuming 0.5 occupancies. An identical view depicting 2Fo-Fc electron density maps of the ferroxidase ligands is shown in Figure S2-B. It is noteworthy that the side chains of E⁵⁰ and D¹²⁹ exhibit two conformations, which allow these residues to bind two iron ions; *i.e.*, E⁵⁰ binds Fe_C and Fe_D and D¹²⁹ binds Fe_D and Fe_E. These observations suggest that the structure is a composite of several populations that enable visualization of the process of iron migration from the ferroxidase center toward the core mineral; the location of Fe_D and Fe_E provide a good idea of the path followed by iron and the multiple conformations of the amino acid side chains involved underscore the role played by side chain coordination and motion in propelling iron along the internal wall of the ferritin molecule. The distance between ferroxidase iron ions (Fe_A and Fe_B) in the pH 6.0 and 7.5 structures is 3.4 Å, which is typical of di-Fe³⁺ sites in di-iron proteins such as ribonucleotide reductase and methane monooxygenase (52). In both Fe-soaked structures Fe_A and Fe_B are bridged by well-defined and spherically symmetric electron density, which was refined as a water molecule, but that could also be a μ-oxo or μ-hydroxo ligand bridging the Fe³⁺ ions. In both structures Fe_C is 10.2 Å from the nearest ferroxidase iron (Fe_B) and 11.2 Å from Fe_A; these distances are larger than those separating Fe_C from Fe_B and Fe_A (~6.3 to 7.4 Å) in the structure of archaeal and bacterial ferritins of known structure. In the pH 7.5 FtnA structure, Fe_D is 8.1 Å from Fe_B and 9.8 Å from Fe_A, whereas Fe_E, which is the iron ion closest to the ferroxidase center, is 7.8 Å from Fe_B and 8.6 Å from Fe_A. The distance between Fe_D and Fe_E is 3.4 Å and the distance between Fe_C and Fe_D is 2.6 Å.

Attempts at emptying the ferroxidase center in crystallo

In a previous report we showed that the ferroxidase center of *Pa* BfrB is readily emptied, in solution, and upon incubation of an iron-soaked crystal in crystallization solution (24). These structural observations and kinetic studies of iron uptake revealed that the ferroxidase center of *Pa* BfrB is likely the dominant port of Fe²⁺ entry into the cavity of *Pa* BfrB (24). In an attempt to learn something about the path followed by iron on its way to the interior of *Pa* FtnA we carried out experiments in which crystals soaked in iron solution were subsequently soaked in crystallization solution that did not contain iron, prior to freezing and data acquisition. Observations made with crystals grown at pH 6.0 are summarized in Figure 5-C: Two features of Fe_B in the double soaked structure are noteworthy, (i) the intensity of its anomalous peak is approximately one half that of Fe_A, and (ii) its position reveals that it is displaced ~1 Å toward the interior cavity relative to Fe_A in the iron-soaked structure. In addition, a “trail” of anomalous electron density can be traced from Fe_B passing through the volume occupied by the imidazole ring of H¹³⁰ and ending at a position similar to that occupied by Fe_E in the pH 7.5 structure; Fe_C is not observed. It is important to note that although difference electron density for the ferroxidase iron ligands is well defined, that corresponding to the imidazole ring in H¹³⁰ can be best described by at least two conformations related by rotation about the C^β-C^γ bond. The electron density (2Fo-Fc) for

the imidazole ring of H¹³⁰ displayed a nearly spherical shape (Figure S2-C), making it difficult to discern its orientation. In addition, positive difference density (Fo-Fc) was observed at the imidazole ring following refinement. The most striking observation, however, is anomalous electron density from iron sharing the same volume in space with electron density from the imidazole ring of H¹³⁰. We interpret these observations to indicate that the data represent a weighted average of several local structures differing in the position of iron as it “trails” from Fe_B toward Fe_E, across the position occupied by the side chain of H¹³⁰ when coordinated to Fe_B. For iron to slide through the position occupied by the H¹³⁰ side chain, the latter has to move out to an alternative conformation. The absence of electron density corresponding to a unique alternative conformation, however, suggests that the side chain populates several conformations rather than a predominant “gate open” conformation. Taken together, the observations strongly suggest that the local structure captured in this snapshot is a composite of several populations that allow visualization of a path followed by Fe_B as it moves toward site C. The results also underscore that iron translocation is made possible by the conformational flexibility of the H¹³⁰ side chain, which may function in a dual role of iron-ligand at the ferroxidase center and iron-gate to allow entry of ferroxidase iron into the interior cavity, as has been shown for the equivalent H¹³⁰ in the ferroxidase center of *Pa* BfrB (24).

Results from similar double soak experiments carried out with crystals grown at pH 7.5 are summarized in Figure 5-D. In this structure, ferroxidase center ions Fe_A and Fe_B exhibit very similar anomalous peak intensities which are nearly twice as intense as that corresponding to Fe_C. The most important difference when compared to the Fe soak structure at pH 7.5 (Figure 5-B) is the absence of Fe_D and Fe_E, which lends support to the idea that these positions correspond to transient iron moving toward the interior cavity, where the last observable stop is Fe_C, before iron is incorporated into the growing mineral. The two conformations observed for D¹²⁹ help preserve the idea that the conformational flexibility of coordinating side chains on the interior surface plays important roles in the internalization of iron. It is also interesting to contrast the relative populations of Fe_A and Fe_B in the Fe-soaked and double soaked structures obtained at pH 6.0 and 7.5. In the Fe soaked structures at both pH values the anomalous peak intensities of the Fe_A and Fe_B ions are nearly identical, which we interpret to indicate nearly full and equal population of the Fe_A and Fe_B sites. The double soak experiments on the other hand, reveal interesting differences: In the pH 7.5 structure, the ferroxidase sites Fe_A and Fe_B appear to remain nearly fully populated, which suggests that at this pH, *in crystallo*, the ferroxidase center of *Pa* FtnA is relatively stable. In comparison, the pH 6.0 structure shows that Fe_B has moved toward the interior cavity and its intensity is approximately one half that of Fe_A, thus suggesting that at pH 6.0, *in crystallo*, ferroxidase iron moves toward the interior, where it is incorporated into the growing mineral. It is important to stress, however, that these crystallographic observations are not sufficient to allow speculation of a mechanism for iron incorporation into *Pa* FtnA; elucidation of such mechanism will require detailed kinetic studies in solution.

Three and four-fold pores

Unlike the three-fold pores of *Ec* FtnA, which are plugged by hydrophobic residues (M¹⁰⁹ and F¹¹⁷) (29), the three-fold pores of *Pa* FtnA are lined with side chains of alternating charge. The outermost layer is formed by the side chains of E¹⁰⁸ and D¹¹⁷ which interact electrostatically with the innermost layer composed of R¹¹⁶ and K¹²⁰. In the pH 6.0 structure a sulfate ion is observed between the two layers of the pore (Figure 6-A and S4), where it is stabilized by electrostatic interactions with the positively charged residues in the inner layer (Figure 6-A); the source of sulfate is the crystallization solution, which contains

200 mM Li_2SO_4 . By comparison, in the pH 7.5 and 10.5 structures the three-fold pores have nearly identical structure, except that water molecules occupy the majority of the volume.

Four-fold pores in *Pa* FtnA assemble at the junction of four subunits (Figure 6-C). Viewed from the exterior the pore perimeter is outlined by the last turn of helix D and by the loop connecting helix D to helix E. The pore walls are formed by a section of helix E, from which stem ligands (N^{148} and Q^{151}) that coordinate a Na^+ ion observed in the four-fold pores of all the structures reported herein, including the Fe-soaked and double soaked structures. The possibility that the metal ion in the four fold pore is iron was eliminated by the absence of anomalous electron density in data sets collected at wavelengths of 1.6314 and 1.7401 Å. In addition, residual difference density, negative or positive, is observed when iron or a water molecule is modeled at these sites, respectively. The presence of Na^+ in the four-fold pores likely stems from the composition of the purification and storage buffers (see experimental). The ligands coordinating the Na^+ ions in the four-fold pores of *Pa* FtnA are identical to those coordinating K^+ observed in the four-fold pores of *Pa* BfrB (24), and Fe^{2+} or Ba^{2+} in bacterioferritin from *Azotobacter vinelandii* (26, 53). In comparison, the four-fold pores of *Ec* FtnA are lined by hydrophilic and hydrophobic residues, with four E^{149} side chains forming the outermost layer, four F^{153} constituting a middle layer and four K^{156} the innermost layer (29). The hydrophilic nature of the residues in the four-fold pores of bacterioferritins from *P. aeruginosa* and *A. vinelandii* is consistent with the crystallographic observation of metal ions bound to the four-fold pores of these structures, observations that have led to the suggestion that Fe^{2+} may traffic in or out of the Bfr cavity via these conduits (24, 26, 53). It is therefore interesting that the structures of the four-fold pores in FtnA, including their avidity for metal ions, are nearly identical to those in the structures of bacterioferritins from *P. aeruginosa* and *A. vinelandii*, because it suggests that Fe^{2+} may also traffic in or out of the *Pa* FtnA structure via the four-fold pores in its structure.

Iron release from *Pa*-FtnA

Experiments directed at studying the mobilization of core iron from *Pa*-FtnA were conducted in an anaerobic glove box using methods described previously for the study of iron release from the core of *Pa* BfrB (22). In brief, the release of iron was initiated by addition of NADPH to a cuvette containing a solution of bipy and *Pa* FtnA mineralized with ~500 iron ions. The process was monitored by following ΔA_{523} , the time-dependent formation of $[\text{Fe}(\text{bipy})_3]^{2+}$. The triangles in Figure 7-A track ΔA_{523} normalized to the total change in absorbance expected upon removal of all the iron ions in the cavity of the ferritin, following addition of NADPH to a solution containing 0.25 μM *Pa* FtnA. The black circles track normalized ΔA_{523} upon addition of NADPH to a mixture of *Pa* FtnA (0.25 μM) and *Pa* Fpr (10 μM). Evidently, *Pa* Fpr is capable of mediating electrons from NADPH to the core of *Pa* FtnA to reduce Fe^{3+} and enable the efficient release of Fe^{2+} from *Pa* FtnA. A pseudo first order rate constant of iron release ($0.092 \pm 0.003 \text{ min}^{-1}$) was estimated from fitting the curve to an exponential function. Results from a similar experiment conducted with a solution containing 0.25 μM *Pa* FtnA, 10 μM *Pa* Fpr and 10 μM apo *Pa* Bfd (apo *Pa* Bfd/*Pa* BfrB ratio =40) are depicted by the open circles in Figure 7-A. This experiment shows a rate of iron release (pseudo first order rate constant = $0.078 \pm 0.004 \text{ min}^{-1}$) similar to that obtained in the absence of apo *Pa* Bfd, thus demonstrating that iron release from *Pa* FtnA is independent of the presence of apo *Pa* Bfd. This behavior is in striking contrast with that previously observed with *Pa* BfrB, which not only requires *Pa* Fpr to mediate electrons from NADPH but also the binding of apo *Pa*-Bfd to release iron (22). To facilitate comparison, in Figure 7-B we show results from similar experiments carried out with *Pa* BfrB mineralized with ~ 550 iron ions: In the absence of apo *Pa* Bfd, addition of NADPH to a solution containing *Pa* BfrB (0.37 μM) and *Pa* Fpr (15 μM) is followed by a slow release of Fe^{2+} (black circles). The rate of Fe^{2+} release, however, can be accelerated in an apo *Pa*

Bfd dependent manner. This is evident from the traces delineated by closed circles, open circles, squares and triangles, which correspond to experiments where the apo *Pa* Bfd/*Pa* BfrB ratio increases from 5, to 15 to 40, respectively, which result in corresponding pseudo first order rate constants of $0.030 \pm 0.001 \text{ min}^{-1}$, $0.058 \pm 0.008 \text{ min}^{-1}$ and $0.101 \pm 0.004 \text{ min}^{-1}$. Clearly, efficient release of iron stored in *Pa* FtnA requires only the input of electrons from *Pa* Fpr, whereas release of iron from *Pa* BfrB requires the presence of apo *Pa* Bfd, in addition to *Pa* Fpr. These observations indicate different regulatory mechanisms for the process of iron release from *Pa* BfrB and from *Pa* FtnA and strongly support the idea that these two distinct types of ferritin-like molecules have specific and likely independent roles in iron management in the cytosol of *P. aeruginosa*.

DISCUSSION

Bacteria have two types of 24-mer ferritin-like molecules, Ftn and Bfr. Although these proteins may play more than one role in the cell, so far it is clear that they participate in iron storage/delivery and in detoxification of the pro-oxidant Fe(II), thereby acting as dynamic regulators of cytosolic iron concentrations. In bacteria harboring both Bfr and Ftn, it is not known which plays a dominant role in iron storage, but it is likely that the significance of their respective participation in iron homeostasis is largely dictated by the environment surrounding the cell. *P. aeruginosa* was thought to harbor only one ferritin-like molecule assembled from two different bacterioferritin subunits, α and β . The idea of a single, mixed chain bacterioferritin in *P. aeruginosa*, however, can be challenged in light of more recent studies showing that the *bfra* and *bfr β* genes appear to be regulated differently (40, 41) and to be expressed independently of one another (9, 40). In this report we present structural and functional evidence supporting the notion that the products of the *bfra* and *bfr β* genes are two distinct ferritins. The product of *bfra* assembles into a 24-mer not capable of binding heme. The structure of its ferroxidase center is similar to the diiron center of bacterial and eukaryotic ferritin in that Fe_A and Fe_B are bridged by only one protein provided ligand (E⁵⁰), which contrasts with the structure of the characteristically symmetric ferroxidase centers of Bfrs, where Fe₁ and Fe₂ are bridged by two glutamate ligands (Figure 1). These structural properties indicate that the product of the *bfra* gene is not a bacterioferritin, but a bacterial ferritin, which we propose should be termed *Pa* FtnA. The ferroxidase center of *Pa* FtnA is fully functional and enables the protein to efficiently capture Fe²⁺, oxidize it and store Fe³⁺ in its core. Although its structure is similar to that seen in *Ec* FtnA, it is not identical because Fe_B in *Pa* FtnA is coordinated by E⁹⁴ and H¹³⁰, whereas that of bacterial and archaeal ferritins of known structure bind Fe_B using two Glu ligands (E⁹⁴ and E¹³⁰ in *Ec* FtnA; see Figure 1). Hence, the chemical environment of Fe_B in *Pa* FtnA imparts its ferroxidase center with a previously unobserved structure.

The structures of *E. coli*, *P. furiosus* and *A. fulgidus* ferritins revealed the presence of a third iron ion near the ferroxidase center, which has been termed site C (Figure 1). The iron soaked structure of *Pa* FtnA at pH 6.0 shows the presence of a third iron ion (Fe_C) in addition to ferroxidase iron. Fe_C in *Pa* FtnA, however, is not completely equivalent to “site C” in *E. coli* and archaeal ferritins because the latter is coordinated by E⁴⁹, E¹²⁶ and E¹²⁹, whereas Fe_C in *Pa* FtnA is coordinated by H⁴⁶ and E⁵⁰ (Figure 5-A). Fe_C was also observed in the iron soaked structure of *Pa* FtnA at pH 7.5 (Figure 5-B), together with the presence of two additional iron ions, Fe_D and Fe_E. In both structures, the anomalous peak intensity defining these iron ions (Fe_C – Fe_E) is roughly one half the anomalous peak intensity corresponding to ferroxidase ions Fe_A and Fe_B, suggesting that these are transient sites in the process of iron translocation from the ferroxidase center to the growing mineral in the interior of the ferritin. The multiple conformations of the side chains coordinating Fe_C - Fe_D add support to this idea because they suggest that iron is propelled along the path delineated by Fe_C, Fe_E and Fe_D by conformational changes of coordinative side chains. The notion

finds additional support in the observations made while attempting to empty the ferroxidase center *in crystallo* by soaking Fe-soaked crystals in crystallization solution at pH 6.0 (Figure 5-C). Particularly revealing are the findings that Fe_B has moved away from its position in the ferroxidase center toward the interior cavity and that an iron ion appears to occupy the same volume in the structure as the side chain of H¹³⁰, because they suggest that internalization of Fe_B along this path requires temporary relocation of the H¹³⁰ side chain.

Placed together, the observations suggest that internalization of an iron ion from the ferroxidase center is facilitated by a gating function of H¹³⁰ in the ferroxidase center of *Pa* FtnA. The path followed by iron on its way to Fe_c may be roughly delineated by a combination of the snapshots provided in Figures 5-B and 5-C. The conformational changes that gate iron entry are likely aided by proton transfer reactions that alter the ionization state of ferroxidase ligands and by electron transfer reactions that change the oxidation state of iron at the ferroxidase center: The distinct conformations of ferroxidase ligands in structures obtained at different pH values (Figure 4) underscore their propensity to respond to local pH changes and highlight a possible role for proton transfer reactions. The dynamic relocation of H¹³⁰ that facilitates internalization of oxidized iron (Figure 5-C and S2-C) suggests that the conformational state of key ferroxidase ligands is also dependent on the oxidation state of iron at the ferroxidase center. Clearly, confirmation of these ideas derived from structural considerations, will have to await kinetic analysis of wild type and judiciously prepared mutants.

Our investigations also show that iron release from *Pa* FtnA and *Pa* BfrB have different regulatory needs (Figure 7). To place these observations in context, it is important to note that iron replete conditions cause strong positive regulation of a *bfrB* gene, whereas iron limitation causes its negative regulation (40). Iron limitation also causes a strong positive regulation of the *bfd* and *fpr* genes (41), which code for a bacterioferritin-associated ferredoxin, and a ferredoxin nicotinamide adenine dinucleotide phosphate reductase, respectively (54), suggesting that the Bfd and Fpr proteins are involved in the process of iron release from BfrB (22). Reconstitution of *Pa* BfrB with *Pa* Fpr *in vitro* causes the iron mineral to be mobilized slowly (black trace in the plot of Scheme 1-A). In contrast, reconstitution of *Pa* BfrB with *Pa* Fpr and apo *Pa* Bfd causes significant acceleration of iron release, as indicated by the red trace. These observations were interpreted to indicate that *Pa* FPR mediates electrons from NADPH to the mineral in *Pa* BfrB via the heme and that interactions between apo *Pa* Bfd and *Pa* BfrB promote the release of iron from *Pa* BfrB (Scheme 1-A) (22). Similar experiments with *Pa* FtnA reveal important differences in the processes of iron release between the two ferritin-like molecules in *P. aeruginosa*: Addition of NADPH to a solution of *Pa* FtnA reconstituted with only *Pa*-Fpr is sufficient to cause rapid release of iron stored in *Pa* FtnA (blue trace in Scheme 1-B). Similar experiments in the presence of apo *Pa* Bfd do not have an appreciable effect on the rate of iron release (Figure 7-A) which indicates that only electrons from a suitable donor can cause efficient mobilization of iron stored in *Pa* FtnA. These contrasting observations add strong support to the notion that *Pa* FtnA and *Pa* BfrB are two distinct ferritins in *P. aeruginosa*.

Supplementary Material

Refer to Web version on PubMed Central for supplementary material.

Acknowledgments

The assistance of Mr. Ritesh Kumar in the preparation of Scheme 1 is acknowledged. Use of IMCA-CAT beamline 17-BM and 17-ID at the Advanced Photon Source was supported by the companies of the Industrial Macromolecular Crystallography Association through a contract with the Hauptman-Woodward Medical Research

Institute. Use of the Advanced Photon Source was supported by the U.S. Department of Energy, Office of Science, Office of Basic Energy Sciences, under Contract No. DE-AC02-06CH11357.

REFERENCES

1. Köster W. ABC Transporter-Mediated Uptake of Iron, Siderophores, Heme and Vitaming B₁₂. Res. Microbiol. 2001; 152:291–301. [PubMed: 11421276]
2. Byers, BR.; Arcenaux, JEL. Microbial Iron Transport: Iron Acquisition by Pathogenic Mircroorganisms. In: Sigel, AaSH., editor. In Metal Ions in Biological Systems. New York: Plenum Press; 1998.
3. Wandersman C, Stojiljkovic I. Bacterial Heme Sources: The Role of Heme, Hemoprotein Receptors and Hemophores. Curr. Oppin. Microbiology. 2000; 3:215–220.
4. Genco CA, Dixon DW. Emerging Strategies in Microbial Haem Capture. Mol. Microbiol. 2001; 39:1–11. [PubMed: 11123683]
5. Andrews SC. Iron Storage in Bacteria. Advan. Microbial Physiol. 1998; 40:281–351.
6. Smith L. The Physiological Role of Ferritin-Like Compounds in Bacteria. Crit. Rev. Microbiol. 2004; 30:173–185. [PubMed: 15490969]
7. Ilari A, Stefanini S, Chiancone E, Tsernoglou D. The Dodecamer Ferritin from *Listeria innocua* Contains a Novel Intersubunit Iron-Binding Site. Nat. Struct. Biol. 2000; 7:38–43. [PubMed: 10625425]
8. Keyer K, Imlay JA. Superoxide Accelerates DNA-Damage by Elevating Free-Iron Levels. Proc. Natl. Acad. Sci. USA. 1996; 93:13635–13649. [PubMed: 8942986]
9. Ma J-F, Ochsner UA, Klotz MG, Nanayakkara VK, Howell ML, Johnson Z, Posey JE, Vasil ML, Monaco JJ, Hassett DJ. Bacterioferritin A Modulates Catalase A (KatA) Activity and Resistance to Hydrogen Peroxide in *Pseudomonas aeruginosa*. J. Bacteriol. 1999; 181:3730–3742. [PubMed: 10368148]
10. Escolar L, Perez-Martin J, De Lorenzo V. Opening the Iron Box: Transcriptional Metalloregulation by the Fur Protein. J. Bacteriol. 1999; 181:6223–6229. [PubMed: 10515908]
11. Ochsner UA, Vasil ML. Gene Repression by the Ferric Uptake Regulator in *Pseudomonas aeruginosa*: Cycle Selection of Iron Regulated Genes. Proc. Natl. Acad. Sci. USA. 1996; 93:4409–4414. [PubMed: 8633080]
12. Wilderman PJ, Sowa NA, FitzGerald DJ, FitGerald PC, Gottesman S, Ochsner UA, Vasil ML. Identification of Tandem Duplicate Regulatory Small RNAs in *Pseudomonas aeruginosa* Involved in Iron Homeostasis. Proc. Natl. Acad. Sci. USA. 2004; 101:9792–9797. [PubMed: 15210934]
13. Wilks A, Burkhard KA. Heme and Virulence: How Bacterial Pathogens Regulate, Transport and Utilize Heme. Nat. Prod. Rep. 2007; 24:511–522. [PubMed: 17534527]
14. Cornelis P, Matthijs S, Van Oeffelen L. Iron Uptake Regulation in *Pseudomonas aeruginosa*. Biometals. 2009; 22:15–22. [PubMed: 19130263]
15. Wyckoff E, Boulette ML, Payne SM. Genetics and Environmental Regulation of *Shigella* Iron Transport Systems. Biometals. 2009; 22:43–51. [PubMed: 19130265]
16. Cornelissen CN, Sparling PF. Iron Piracy: Acquisition of Transferrin-Bound Iron by Bacterial Pathogens. Mol. Microbiol. 1994; 14:843–850. [PubMed: 7715446]
17. Vasil ML, Ochsner UA. The Response of *Pseudomonas aeruginosa* to Iron: Genetics, Biochemistry and Virulence. Mol. Microbiol. 1999; 34:399–413. [PubMed: 10564483]
18. Vasil ML. How We Learnt About Iron Acquisition in *Pseudomonas aeruginosa*: A Series of Very Fortunate Events. Biometals. 2007; 20:587–601. [PubMed: 17186376]
19. Liu X, Theil EC. Ferritins: Dynamic Management of Biological Iron and Oxygen Chemistry. Acc. Chem. Res. 2005; 38:167–175. [PubMed: 15766235]
20. Andrews SC. The Ferritin-Like Superfamily: Evolution of the Biological Iron Storeman from a Rubrerythrin-Like Ancestor. Biochim. et Biophys. Acta. 2010; 1800:691–705.
21. Le Brun NE, Crow A, Murphy MEP, Mauk AG, Moore GR. Iron Core Mineralization in Prokaryotic Ferritins. Biochim. et Biophys. Acta. 2010; 1800:732–744.
22. Weeratunga S, Gee CE, Lovell S, Zeng Y, Woodin CL, Rivera M. Binding of *Pseudomonas aeruginosa* Apobacterioferritin-Associated Ferredoxin to Bacterioferritin B Promotes Heme

- Mediation of Electron Delivery and Mobilization of Core Mineral Iron. *Biochemistry*. 2009; 48:7420–7431. [PubMed: 19575528]
23. Andrews SC. The Ferritin-like Superfamily: Evolution of the Biological Iron Storeman from a Ruberythrin-Like Ancestor. *Biochim. et Biophys. Acta*. 2010; 1800:691–705.
 24. Weeratunga S, Lovell S, Yao H, Battaile KP, Fischer CJ, Gee CE, Rivera M. Structural Studies of Bacterioferritin B (BfrB) from *Pseudomonas aeruginosa* Suggest a Gating Mechanism for Iron Uptake via the Ferroxidase Center. *Biochemistry*. 2010; 49:1160–1175. [PubMed: 20067302]
 25. Crow A, Lawson TL, Lewin A, Moore GR, Le Brun NE. Structural Basis for Iron Mineralization by Bacterioferritin. *J. Am. Chem. Soc.* 2009; 131:6808–6813. [PubMed: 19391621]
 26. Swartz L, Kuchinkas M, Li H, Poulos TL, Lanzilotta WN. Redox-Dependent Structural Changes in the *Azotobacter vinelandii* Bacterioferritin: New Insights into the Ferroxidase and Iron Transport Mechanism. *Biochemistry*. 2006; 45:4421–4428. [PubMed: 16584178]
 27. Macedo S, Romão CV, Mitchell E, Matias PM, Liu MY, Xavier AV, LeGall J, Teixeira M, Lindley P, Carrondo MA. The Nature of the Di-Iron Site in the Bacterioferritin from *Desulfovibrio desulfuricans*. *Nat. Struct. Biol.* 2003; 10:285–290. [PubMed: 12627224]
 28. Janowski R, Auerbach-Nevo T, Weiss MS. Bacterioferritin from *Mycobacterium smegmatis* Contains Zinc in its Di-Nuclear Site. *Prot. Sci.* 2007; 17:1138–1150.
 29. Stillman TJ, Hempstead PD, Artymiuk PJ, Andrews SC, Hudson AJ, Treffry JR, Guest PM, Harrison PM. The High-Resolution X-ray Crystallographic Structure of the Ferritin (EcFtnA) of *Escherichia coli*; comparison with human H Ferritin (HuHF) and the Structures of the Fe³⁺ and Zn²⁺ Derivatives. *J. Mol. Biol.* 2001; 307:587–603. [PubMed: 11254384]
 30. Cho KJ, Shin HJ, Lee J-H, Kim K-J, Park SS, Lee Y, Lee C, Park SS, Kim KH. The Crystal Structure of Ferritin from *Helicobacter pylori* Reveals Unusual Conformational Changes for Iron Uptake. *J. Mol. Biol.* 2009; 390:83–98. [PubMed: 19427319]
 31. Tatur J, Hagen WR, Matias PM. Crystal Structure of the Ferritin from the Hyperthermophilic Archaeal Anaerobic *Pyrococcus furiosus*. *J. Biol. Inorg. Chem.* 2007; 12:615–630. [PubMed: 17541801]
 32. Johnson E, Cascio D, Sawaya MR, Gingery M, Schroder I. Crystal Structures of a Tetrahedral Open Pore Ferritin from the Hyperthermophilic Archaeon *Archaeoglobus fulgidus*. *Structure*. 2005; 13:637–648. [PubMed: 15837202]
 33. Treffry A, Zhao Z, Qail MA, Guest JR, Harrison PM. how the Presence of Three Iron Binding Sites Affects the Iron Storage Function of the Ferritin (EcFtnA) of *Escherichia coli*. *FEBS Letters*. 1998; 432:213–218. [PubMed: 9720927]
 34. Moore GR, Mann S, Bannister JV. Isolation and Properties of the Complex Nonheme-Iron-Containing Cytochrome *b₅₅₇* (Bacterioferritin) from *Pseudomonas aeruginosa*. *J. Inorg. Biochem.* 1986; 28:329–336. [PubMed: 3100721]
 35. Moore GR, Kadir HA, Al-Massad K, Le Brun NE, Thomson AJ, Greenwood C, Keen JN, Findlay JBC. Structural Heterogeneity of *Pseudomonas aeruginosa* Bacterioferritin. *Biochem J.* 1994; 304:493–497. [PubMed: 7998985]
 36. Andrews SC, Harrison PM, Guest JR. Cloning, Sequencing, and Mapping of the Bacterioferritin Gene (*bfr*) of *Escherichia coli* K-12. *J. Bacteriol.* 1989; 171:3940–3947. [PubMed: 2661540]
 37. Garg RP, Vargo CJ, Cui X, Kurtz DMJ. A [2Fe-2S] Protein Encoded by an Open Reading Frame Upstream of the *Escherichia coli* Bacterioferritin Gene. *Biochemistry*. 1996; 35:6297–6301. [PubMed: 8639572]
 38. Quail MA, Jordan P, Grogan JM, Butt JN, Lutz M, Thomson AJ, Andrews SC, Guest JR. Spectroscopic and Voltammetric Characterization of Bacterioferritin-Associated Ferredoxin of *Escherichia coli*. *Biochem. Biophys. Res. Commun.* 1996; 229:635–642. [PubMed: 8954950]
 39. Stover CK, Pham XQ, Erwin AL, Mizoguchi SD, Warriner P, Hickey MJ, Brinkman FSL, Hufnagle WO, Kowalik DJ, Lagrou M, Garber RL, Goltry L, Tolentino E, Westbrook-Wadman S, Yuan Y, Brody LL, Coulter SN, Folger KR, Kas A, Larbig K, Lim R, Simith K, Spencer D, Wong GKS, Wu Z, Paulsen IT, Reizer J, Saler MH, Hancock REW, Lory S, Olson MV. Complete Genome Sequence of *Pseudomonas aeruginosa* PA01, an Opportunistic Pathogen. *Nature*. 2000; 406:959–964. [PubMed: 10984043]

40. Palma M, Worgall S, Quadri LEN. Transcriptome Analysis of the *Pseudomonas aeruginosa* Response to Iron. Arch. Microbiol. 2003; 180:374–379. [PubMed: 14513207]
41. Ochsner UA, Wilderman PJ, Vasil AI, Vasil ML. GeneChip Expression Analysis of the Iron Starvation Response in *Pseudomonas Aeruginosa*: Identification of Novel Pyoverdine Biosynthesis Genes. Mol. Microbiol. 2002; 45:1277–1287. [PubMed: 12207696]
42. Ikemura T. Codon Usage and tRNA Content in Unicellular and Multicellular Organisms. Mol. Biol. Evol. 1985; 2:13–34. [PubMed: 3916708]
43. Ringeling PL, Davy SL, Monkara FA, Hunt C, Dickson DPE, McEwan AG, Moore GR. Characterization of Bacterioferritin and Formation of Non-Haem Iron Particles in Intact Cells. Eur. J. Biochem. 1994; 223:847–855. [PubMed: 8055962]
44. Otwinowski Z, Minor W. Processing of X-ray Diffraction Data Collected in Oscillation Mode. Methods Enzymol. 1997; 276:307–326.
45. Kabsch W. Automatic indexing of rotation diffraction patterns. Journal of Applied Crystallography. 1988; 21:67–72.
46. Evans P. Scaling and assessment of data quality. Acta Crystallogr D Biol Crystallogr. 2006; 62:72–82. [PubMed: 16369096]
47. Vagin A, Teplyakov A. *MOLREP*: an Automated Program for Molecular Replacement. J. Appl. Cryst. 1997; 30:1022–1025.
48. Adams PD, Afonine PV, Brunkóczy G, Chen VB, Davis IW, Echols N, Headd JJ, Hung L-W, Kapral GJ, Grosse-Kunstleve RW, McCoy AJ, Moriarty NW, Oeffner R, Read RJ, Richardson DC, Richardson JS, Terwilliger TC, Zwart PH. PHENIX: A Comprehensive Python-Based System for Macromolecular Structure Solution. Acta Cryst. 2010; D66
49. Emsley P, Cowtan K. Coot: model-building tools for molecular graphics. Acta Crystallogr D Biol Crystallogr. 2004; 60:2126–2132. [PubMed: 15572765]
50. Lovell SC, Davis IW, Arendall WBr, de Bakker PI, Word JM, Prisant MG, Richardson JS, Richardson DS. Structure Validation by C-Alpha Geometry: Phi, Psi and C-Beta Deviation. Proteins. 2003; 30:437–450. [PubMed: 12557186]
51. Chen VB, Arendall WBr, Headd JJ, Keedy DA, Immormino RM, Kapral GJ, Murray LW, Richardson JS, Richardson DC. MolProbity: All-Atom Structure Validation for Macromolecular Crystallography. Acta Cryst. 2010; D 66:12–21.
52. Kurtz DM. Structural Similarity and Functional Diversity of Diiron-Oxo Proteins. J. Biol. Inorg. Chem. 1997; 2:159–167.
53. Liu H-L, Zhou H-N, Xing W-M, Zhao J-F, Li S-X, Huang J-F, Bi R-C. 2.6 Å Resolution Crystal Structure of the Bacterioferritin from *Azotobacter vinelandii*. FEBS Lett. 2004; 573:93–98. [PubMed: 15327981]
54. Wang A, Zeng Y, Han H, Weeratunga S, Morgan BN, Moënné-Loccoz P, Schönbrunn E, Rivera M. Biochemical and Structural Characterization of *Pseudomonas aeruginosa* Bfd and FPR: Ferredoxin NADP⁺ Reductase and Not Ferredoxin is the Redox Partner of Heme Oxygenase under Iron-Starvation Conditions. Biochemistry. 2007; 46:12198–12211. [PubMed: 17915950]
55. Diederichs K, Karplus PA. Improved R-factors for Diffraction Data Analysis in Macromolecular Crystallography. Nat. Struct. Biol. 1997; 4:269–275. [PubMed: 9095194]
56. Lawson DM, Artymiuk PJ, Yewdall SJ, Smith JA, Livingstone JC, Treffry A, Luzzago A, Levi S, Arosio P, Cesareni G, Thomas CD, Shaw WV, Harrison PM. Solving the Structure of Human H Ferritin by Genetically Engineering Intermolecular Crystal Contacts. Nature. 1991; 349:541–544. [PubMed: 1992356]

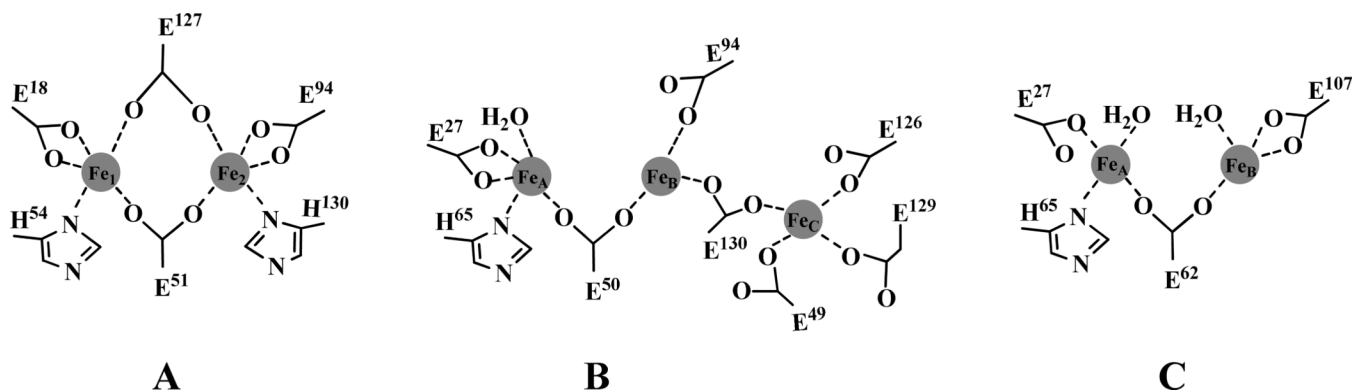


Figure 1.

Schematic representation of the (A) symmetrical ferroxidase center typical of bacterioferritin (Bfr) where Fe_1 and Fe_2 are bridged by two Glu residues; numbering as in *Pa* BfrB. (B) ferroxidase center seen in *E. coli* and archaeal Ftn (see text); “site C” (Fe_C) is included in addition to ferroxidase iron Fe_A and Fe_B and numbering is as in *Ec* FtnA. (C) ferroxidase center of human H-ferritin adapted from the crystal structure of its Tb^{3+} derivative (56).

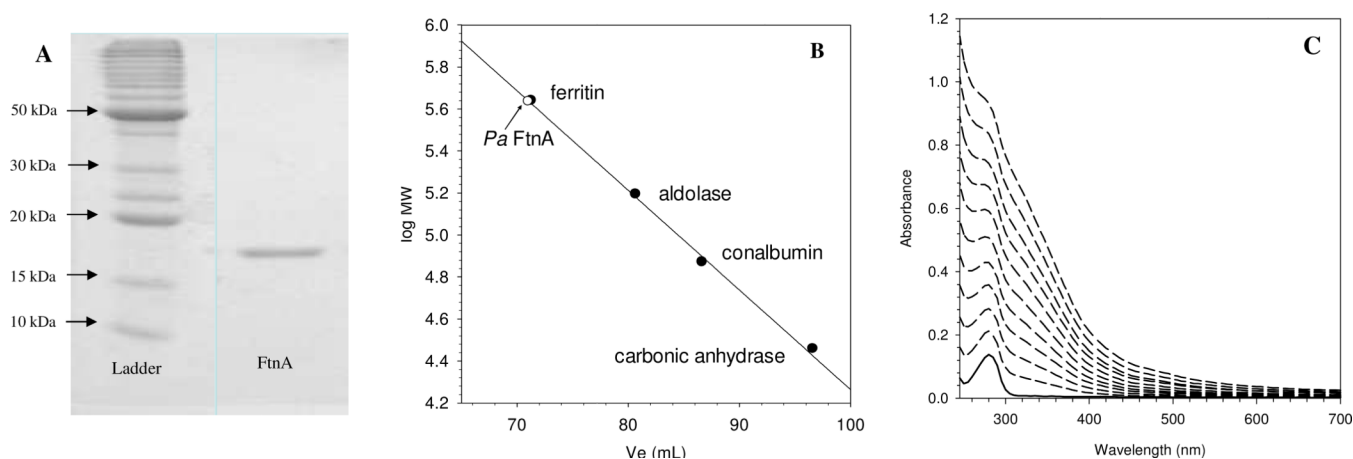


Figure 2. Characterization of recombinant *Pa FtnA*. (A) 15% SDS PAGE analysis of *Pa FtnA* purified to homogeneity. (B) Calibration curve obtained to estimate the molecular mass of 24-mer *Pa FtnA* was constructed from the elution volume (V_e) of ferritin (440 kDa), aldolase (158 kDa), conalbumin (75 kDa), and carbonic anhydrase (29 kDa) loaded onto a Superdex 200 column equilibrated with 50 mM sodium phosphate pH 7.4. (C) Family of spectra obtained during the reconstitution of core iron mineral in recombinant *Pa FtnA* (0.2 μ M in 50 mM TRIS, pH 7.4); the spectrum with the continuous line, obtained prior to addition of Fe^{2+} , is compared with spectra obtained after subsequent addition of Fe^{2+} aliquots

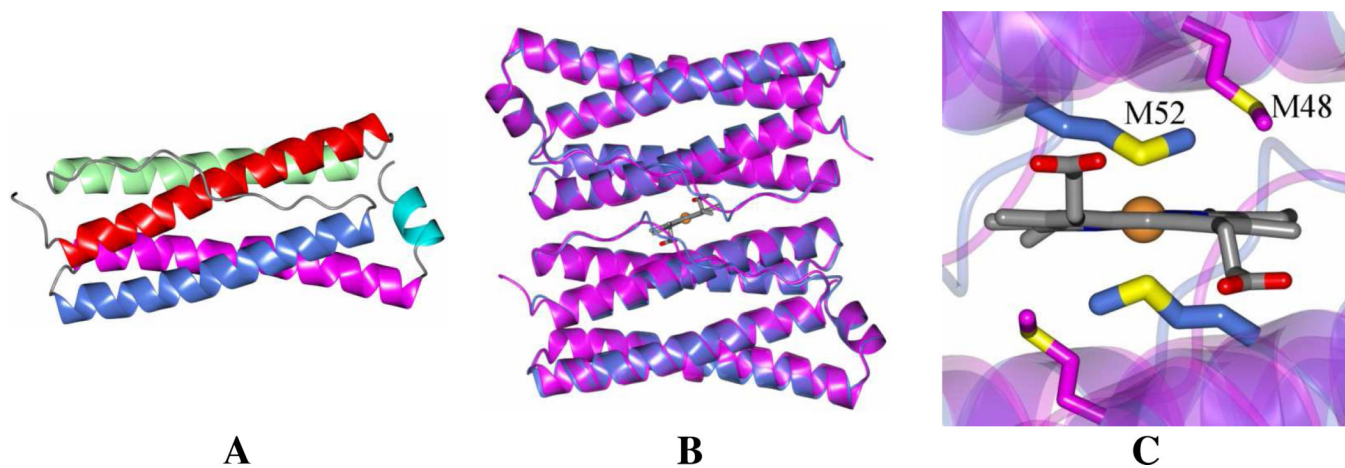


Figure 3.

(**A**) Secondary structure of *Pa* FtnA showing helices A (red), B (green), C (blue) D (magenta) and E (cyan). (**B**) Superposition of a *Pa* BfrB non-crystallographic dimer (blue, PDB: 3IS7) and a *Pa* FtnA crystallographic dimer (magenta); view is along the 2-fold axis. The heme from *Pa* BfrB is shown in grey. (**C**) Zoomed-in view showing M⁵² of *Pa* BfrB binding heme (blue) and the relative position of the closest Met residue in *Pa* FtnA, M⁴⁸.

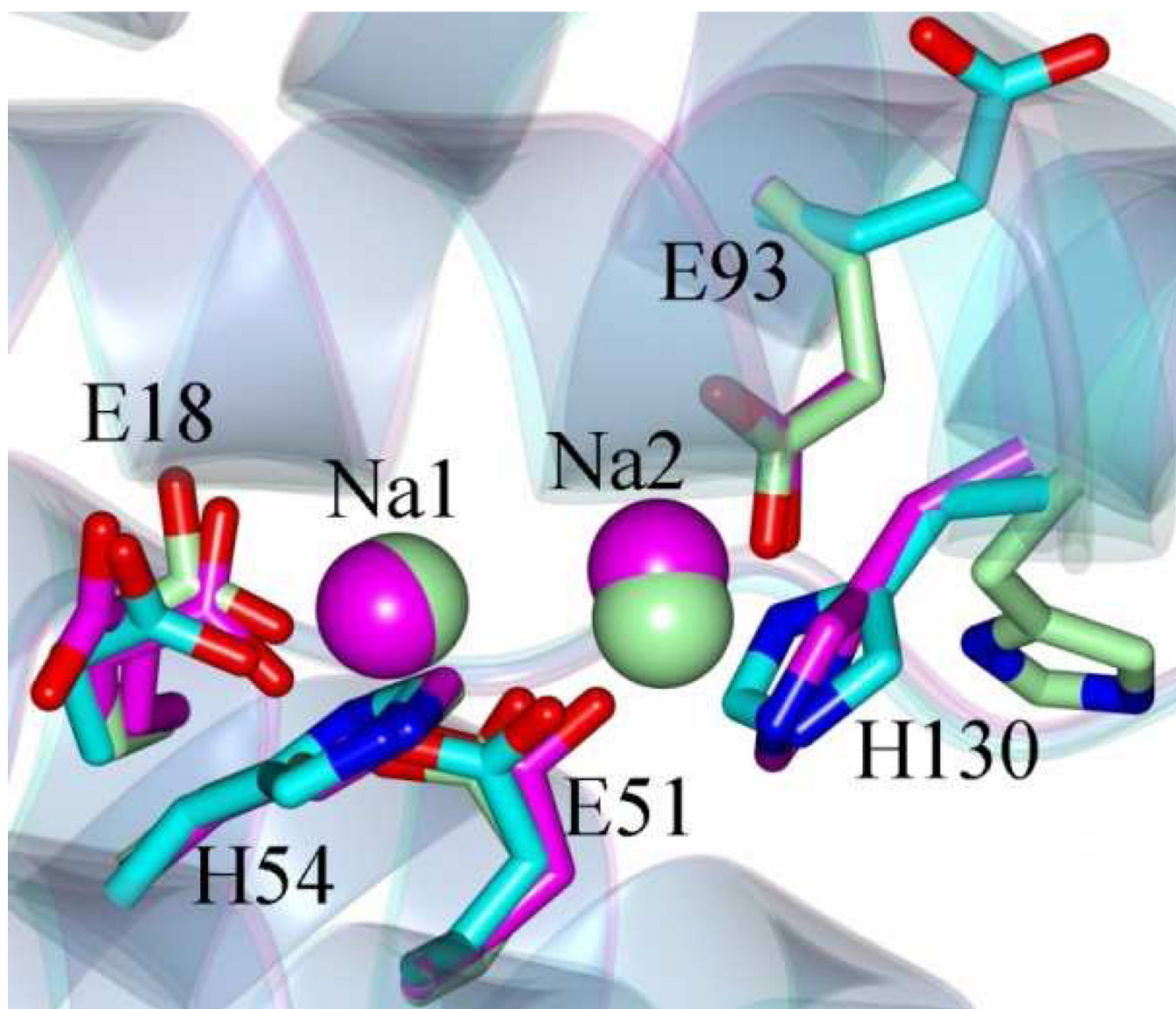


Figure 4. Superposition of as isolated *Pa* FtnA structures obtained from crystals grown at pH 6.0 (cyan), pH 7.5 (magenta) and pH 10.5 (green) showing the ferroxidase center. Sodium ions are drawn as spheres.

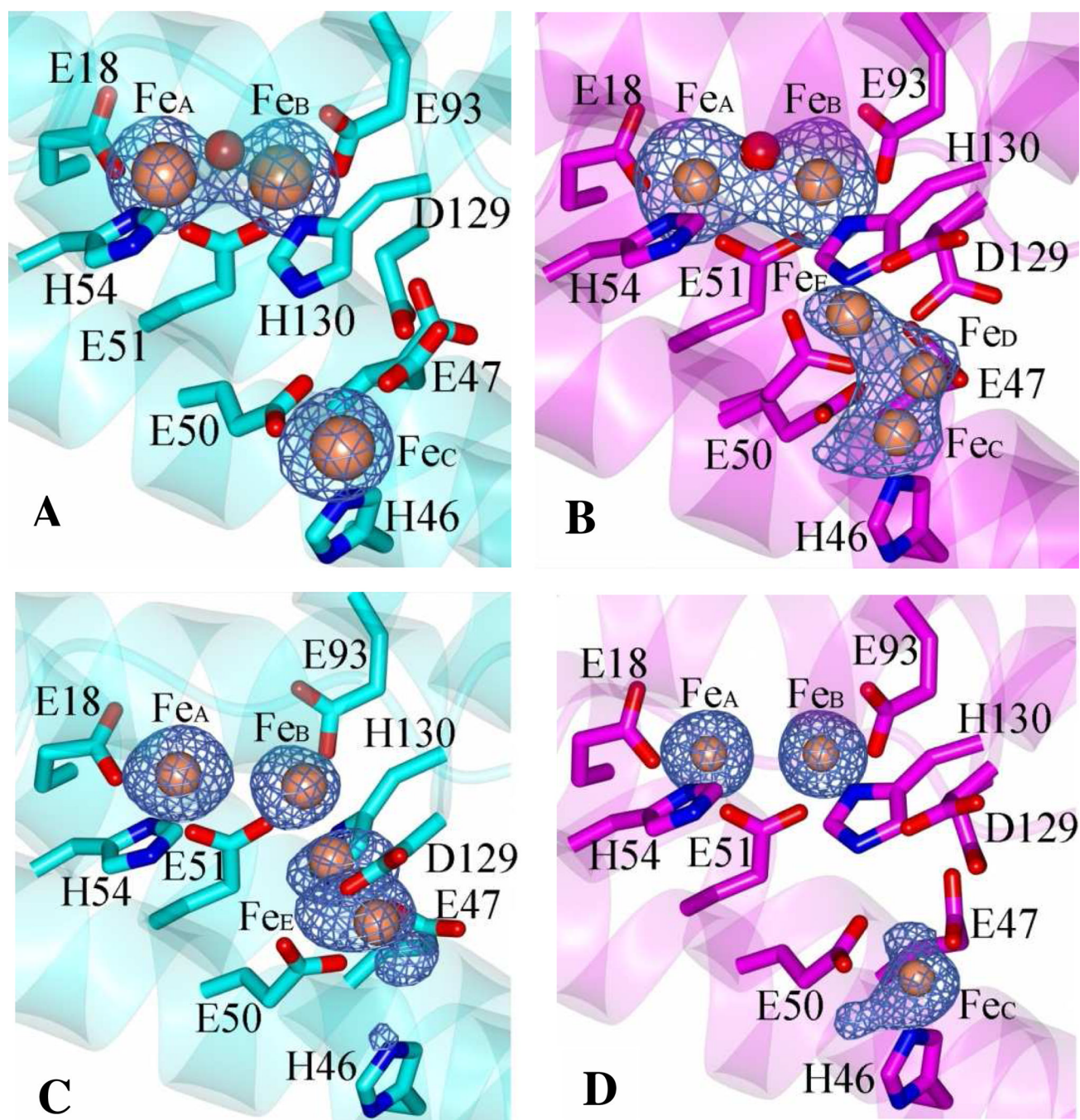


Figure 5. Phased anomalous difference maps (blue mesh) of the ferroxidase center of *Pa* FtnA Fe soaked and double soaked contoured at 5σ . **(A)** pH 6.0 Fe soak ($\lambda = 1.7401\text{\AA}$), **(B)** pH 7.5 Fe soak ($\lambda = 1.6531\text{\AA}$), **(C)** pH 6.0 double soaked ($\lambda = 1.7401\text{\AA}$), and **(D)** pH 7.5 double soaked ($\lambda = 1.7401\text{\AA}$). Identical views depicting 2Fo-Fc electron density maps of the ferroxidase iron ligands are shown in Figure S2.

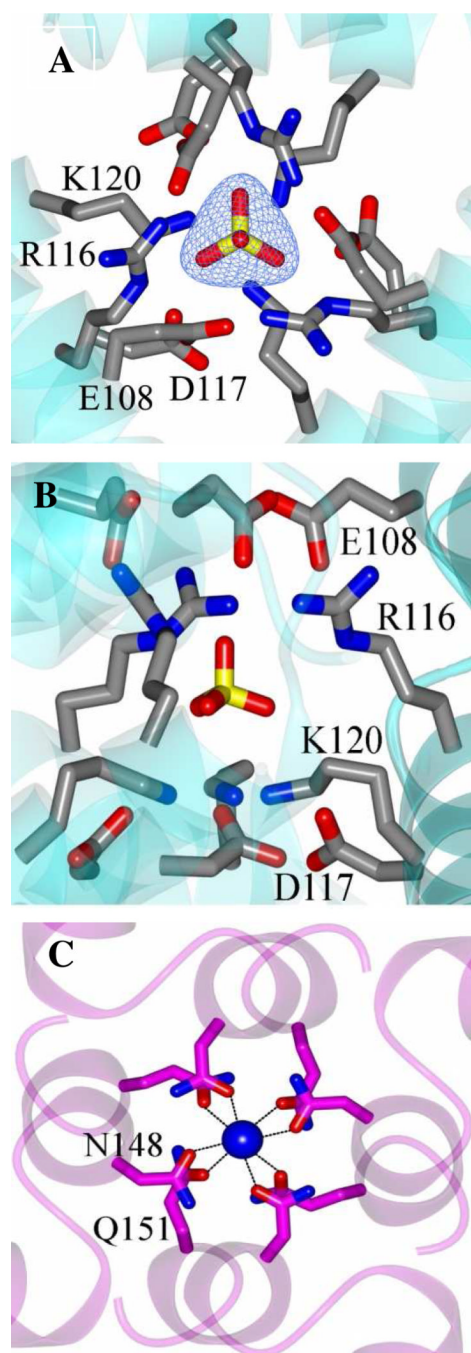


Figure 6.

(A) View along a 3-fold pore in *Pa* FtnA (pH 6.0) showing a sulfate ion (yellow) positioned between an inner layer of positively charged residues R¹¹⁶ and K¹²⁰; negatively charged residues E¹⁰⁸ and D¹¹⁷ occupy the outer layer. The 2Fo-Fc electron density map for the sulfate ion, contoured at 1σ, is shown as blue mesh. (B) View normal to the 3-fold pore axis showing the layers of positively and negatively charged residues. (C) View of a 4-fold pore in *Pa* FtnA (pH 6.0) showing the residues that coordinate a sodium ion (blue sphere).

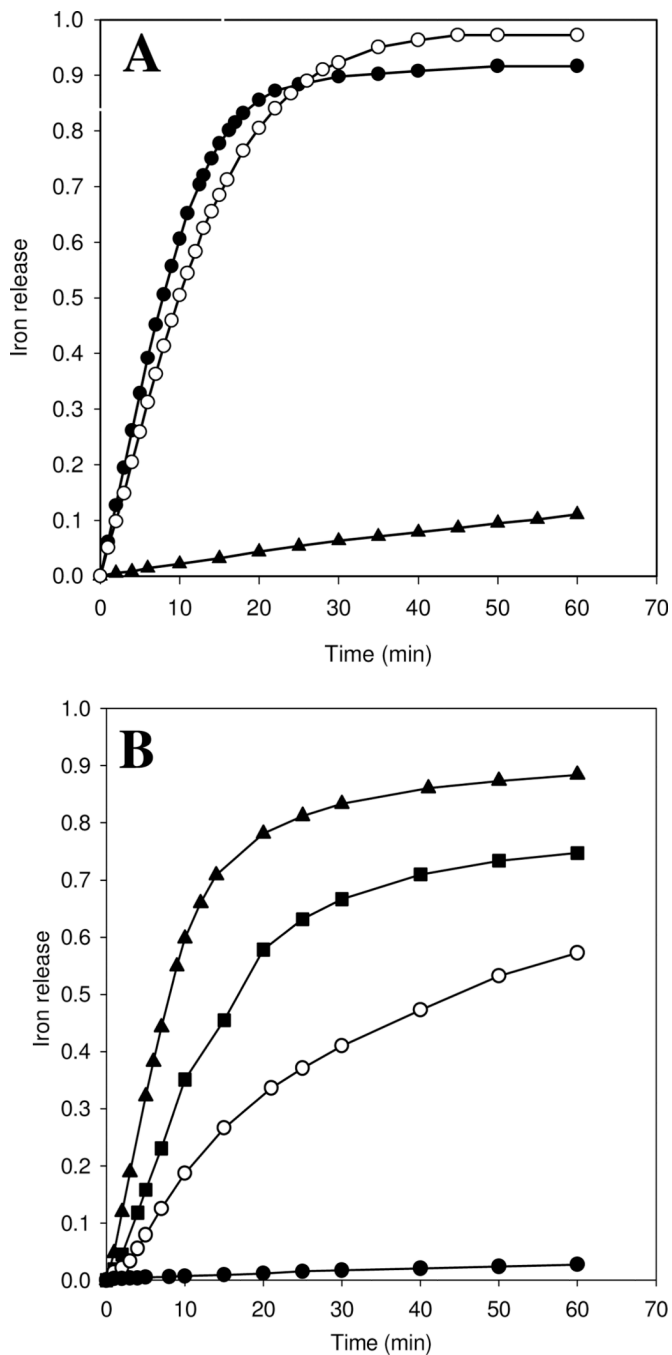
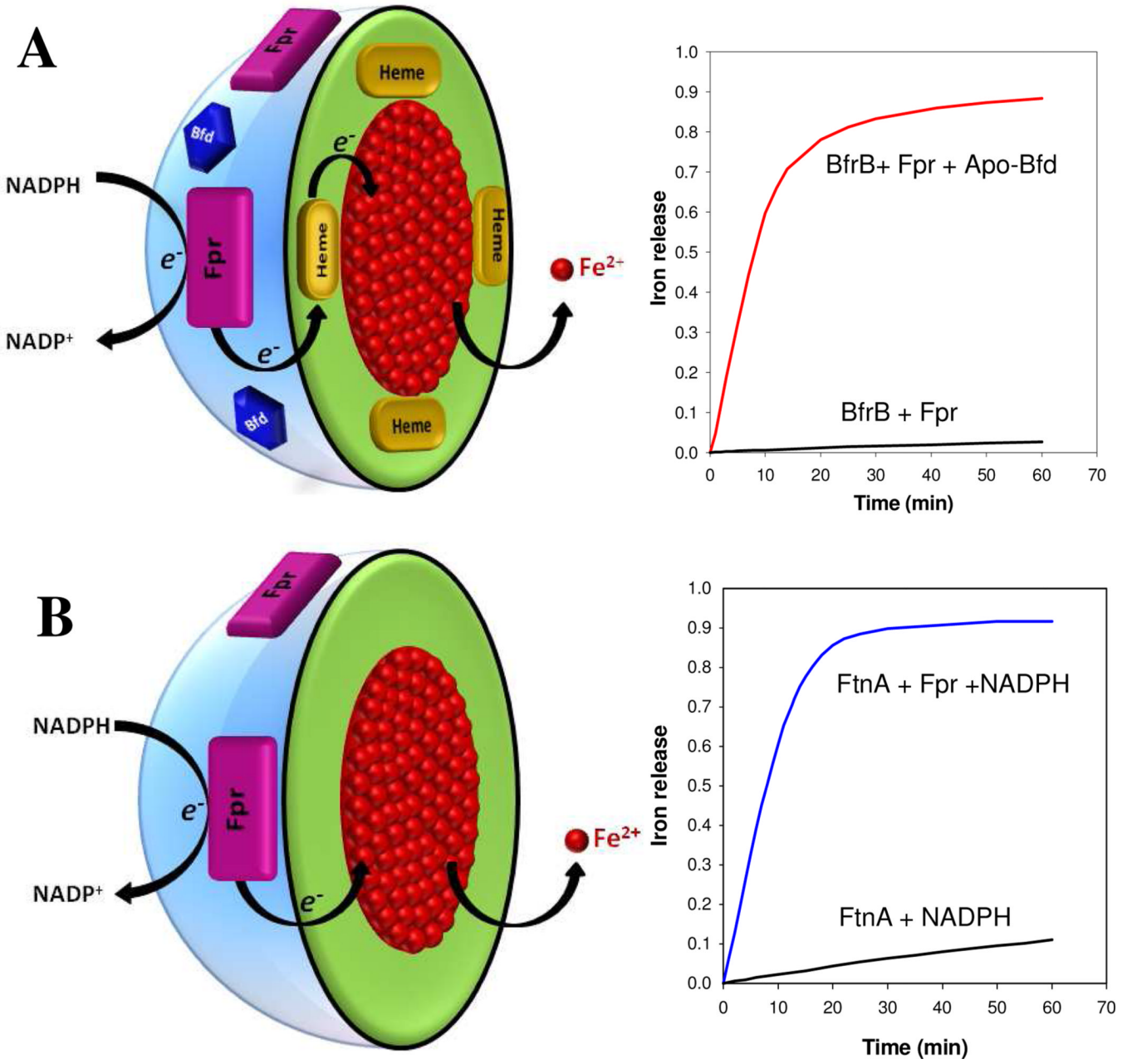


Figure 7. Iron release from *Pa* FtnA and from *Pa* BfrB has different regulatory needs. (A) Time-dependent increase in normalized ΔA^{523} upon addition of excess NADPH (1.5 mM final concentration) to 20 mM phosphate buffer (pH 7.6) containing: (▲) *Pa* FtnA (0.25 μ M), (○) *Pa* FtnA (0.25 μ M) and *Pa* Fpr (10 μ M), and (●) *Pa* FtnA (0.25 μ M), *Pa* Fpr (10 μ M) and apo *Pa* Bfd (10 μ M); the apo Bfd/FtnA ratio is 40. (B) Time dependent increase in normalized ΔA^{523} upon addition of excess NADPH (1.5 mM final concentration) to a solution containing *Pa* BfrB (0.37 μ M), *Pa* Fpr (15 μ M) and apo *Pa* Bfd with Bfd/BfrB molar ratio of 0 (●), 5 (○), 15 (■) and 40 (▲).



Scheme 1.
Distinct requirements for the release of iron stored in *Pa* BfrB and *Pa* FtnA

Table 1

Crystallographic data for *Pa* FtnA structures.

	Apo (pH 6.0)	Fe Soaked (pH 6.0)	Double Soak (pH 6.0)	Apo (pH 7.5)	Fe Soaked (pH 7.5)	Double Soak (pH 7.5)	Apo (pH 10.5)
Data Collection							
Unit-cell parameters (Å)	$a=171.34$	$a=170.73$	$a=171.16$	$a=172.59$	$a=172.52$	$a=173.27$	$a=173.12$
Space group	F432	F432	F432	F432	F432	F432	F432
Resolution ^I (Å)	98.92-1.95 (2.06-1.95)	98.57-1.65 (1.74-1.65)	98.82-2.10 (2.21-2.10)	30.0-1.55 (1.61-1.55)	30.0-1.85 (1.92-1.85)	100.04-1.80 (1.90-1.80)	29.25-1.70 (1.79-1.70)
Wavelength (Å)	1.7401	1.7401	1.7401	1.0000/1.6531	1.0000/1.6531	1.7401	1.0000
Observed reflections	595,243	745,089	486,834	472,881	204,183	687,618	1,026,694
Unique reflections	16,285	25,503	13,093	32,338	19,371	21,231	24,998
$\langle I/\sigma(I) \rangle$	30.2 (4.9)	20.8 (2.0)	33.0 (5.9)	42.9 (2.7)	33.4 (2.2)	23.3 (2.6)	27.6 (5.2)
Completeness ^I (%)	100.0 (100.0)	97.3 (81.2)	100.0 (100.0)	99.4 (99.8)	99.9 (100)	100.0 (100.0)	100 (100)
Multiplicity ^I	36.6 (34.5)	29.2 (4.0)	37.2 (37.9)	14.6 (14.7)	10.5 (10.3)	32.4 (16.2)	41.1 (36.6)
R_{merge}	9.0 (84.9)	12.2 (58.8)	8.6 (76.5)	5.8 (72.4)	6.4 (80.5)	10.2 (88.4)	15.0 (87.0)
R_{pim} (%) ^{I, 4}	1.5 (14.6)	2.1 (29.6)	1.5 (12.7)	N/A	N/A	1.8 (22.7)	2.4 (14.5)
Refinement							
Resolution (Å)	98.92-1.95	60.36-1.65	51.61-2.10	24.17-1.55	26.00-1.85	52.24-1.80	28.85-1.70
Reflections (working/test)	15,463/ 819	24,198/1,293	12,451/641	30,356/1,615	18,364/990	20,133/1,091	23,718/1,274
$R_{\text{factor}}/R_{\text{free}}$ (%) ³	18.9/23.2	15.5/18.3	19.4/25.1	18.0/20.6	17.9/22.8	17.5/20.3	15.3/17.6
No. of atoms (protein/Fe/ Na/SO ₄ /water)	1,258/0/18/96	1,294/3/13/178	1,269/4/13/64	1,299/0/3/0/164	1,295/5/10/134	1,284/3/10/185	1,279/0/3/0/179
Model Quality							
R.m.s deviations							
Bond lengths (Å)	0.019	0.014	0.016	0.020	0.017	0.014	0.016
Bond angles (°)	1.482	1.416	1.460	1.221	1.420	1.294	1.373
Average <i>B</i> factor (Å ²)							
All Atoms	34.2	16.9	38.3	17.6	25.4	25.0	14.7
Protein	33.5	15.2	37.9	16.1	24.4	23.6	13.0
Water	42.2	28.7	43.9	17.6	24.3	34.3	25.0

	Apo (pH 6.0)	Fe Soaked (pH 6.0)	Double Soak (pH 6.0)	Apo (pH 7.5)	Fe Soaked (pH 7.5)	Double Soak (pH 7.5)	Apo (pH 10.5)
Iron/Sodium	-/31.2	27.1/11.9	62.0/46.0	-/16.1	40.1/38.3	47.7/44.8	-/18.0
Sulfate	43.9	24.2	44.0	-	-	-	-
Coordinate error based on maximum likelihood (Å)	0.22	0.14	0.20	0.18	0.18	0.23	0.15
Ramachandran Plot							
Favored (%)	98.7	99.4	99.3	98.8	98.7	98.7	99.4
Additionally allowed (%)	1.3	0.6	0.7	1.2	1.1	1.3	0.6

1) Values in parenthesis are for the highest resolution shell.

2) $R_{\text{merge}} = \frac{\sum_{hk} \sum_i |I_i(hkl) - \langle I(hkl) \rangle|}{\sum_{hk} \sum_i I_i(hkl)}$, where $I_i(hkl)$ is the intensity measured for the i th reflection and $\langle I(hkl) \rangle$ is the average intensity of all reflections with indices hkl .

3) $R_{\text{factor}} = \frac{\sum_{hk} \|F_{\text{obs}}(hkl) - |F_{\text{calc}}(hkl)|\|}{\sum_{hk} \|F_{\text{obs}}(hkl)\|}$; R_{free} is calculated in an identical manner using 5% of randomly selected reflections that were not included in the refinement

4) R_{prim} = precision-indicating (multiplicity-weighted) R_{merge} (55)